Composites Science and Technology 273 (2026) 111401

Contents lists available at ScienceDirect

Composites Science and Technology

journal homepage: www.elsevier.com/locate/compscitech

Investigation of mechanical properties and transverse crack onset of thin-ply carbon-fiber composites in ambient and cryogenic conditions with varying fiber types

Eduardo Szpoganicz [a], Fabian Hübner [b], Uwe Beier [b], Edgard Boutant [a], Holger Ruckdäschel [a,*]

[a] Department of Polymer Engineering, University of Bayreuth, Bayreuth, Germany
[b] Airbus Central Research and Technology, Munich, Germany

ARTICLE INFO

Keywords:
Carbon fiber
Thin-plies
Cryogenic testing
Transverse crack
Interlaminar toughness
LaRC03

ABSTRACT

Transverse microcracking is a critical failure mode in carbon fiber-reinforced polymers (CFRPs) used in linerless cryogenic storage systems, yet reliable prediction of crack onset in cryogenic environments remains challenging. This study investigates CFRP laminates with different fiber moduli and ply thicknesses, and applies the LaRC03 embedded ply failure criterion to predict transverse crack initiation at 296 K and 77 K. The necessary engineering constants (energy release rates, tensile moduli, shear moduli) were measured for each system in both environments and used in the model. Results show that intermediate modulus fibers provide the best balance of toughness and modulus, providing the greatest resistance to 90° ply microcracking under cryogenic conditions. High-tenacity fibers improve resistance to opening-mode cracks but are more prone to shear-driven damage, especially at 296 K where deformation levels are higher. High-modulus fibers presented lower transverse crack onset strength in both environments due to inherent brittleness. Fiber diameter also affects crack initiation through its influence on the ply thickness-to-fiber diameter ratio. The LaRC03 model correlated well with experimental results in both environments, with greater agreement for laminates at 77 K testing.

1. Introduction

Developing materials capable of maintaining structural integrity in cryogenic environments has become an active area of research across next-generation propulsion systems. From clean commercial aviation [1,2] to space launch vehicles [3,4], resilience and long-term performance of cryogenic storage systems under fluctuating thermal conditions are key aspects for reliable operation. To reduce structural mass and improve overall vehicle efficiency, industry is investigating linerless carbon-fiber reinforced polymer (CFRP) composites for the storage of cryogenic fuels [5,6]. CFRPs are attractive due to their high strength, lightweight, and durability. However, when used as structural materials for cryogenic fuel tanks, they must withstand extremely low temperatures, with liquid hydrogen at 20 K and liquid oxygen at 90 K. At these conditions, the polymer matrix becomes brittle and susceptible to microcrack propagation, which reduces the effectiveness of CFRP structures [5–9]. Preventing leakage in CFRP tanks remains a major challenge, particularly in linerless systems, where the composite wall itself is directly exposed to cryogenic fuels. Transverse microcracks are especially critical because they can grow through the laminate and form leakage paths, ultimately compromising tank integrity [5,10].

Simply cooling CFRP laminates to cryogenic temperatures can lead to microcracking. Timmermann [7,8] studied how cryogenic cycling affects CFRP crossply laminates. It was found that higher matrix modulus reduced microcracking [7], and that improved fiber-matrix adhesion (achieved through surfactant-sized fibers) increased resistance [8]. Johnson et al. [9] tested IM7/977-2 laminates at room temperature (RT) and 77 K, finding no major decline in delamination toughness. More recent studies have focused on CFRPs with cryogenic-specific matrices [10–17]. Hohe et al. [10,11] tested static modulus and strength in liquid helium (4 K), observing thermal residual stresses from mismatched ply orientations [10]. Puck's failure criterion did not apply, as modulus did not change significantly [11]. Wang et al. [12] tested T700 and T800 CFRPs at 77 K using a cryogenic epoxy matrix and found increased tensile and compressive strength compared to RT. Li et al. [13] developed a multiscale model for CFRP behavior at 93 K, providing useful insights into damage evolution in combination with thermal stress for low temperature conditions.

* Corresponding author. University of Bayreuth, Polymer Engineering, Universitätstr. 30, 95447, Bayreuth, Germany
E-mail address: ruckdaeschel@uni-bayreuth.de (H. Ruckdäschel).

https://doi.org/10.1016/j.compscitech.2025.111401
Received 25 August 2025; Received in revised form 1 October 2025; Accepted 4 October 2025
Available online 8 October 2025

At cryogenic temperatures, the matrix exhibits significantly lower failure strain, making crack growth and overall failure more dependent on matrix ductility than on the composite's global strength. Hübner et al. [14,15] studied toughened epoxy-amine systems at low temperatures for type V vessels. As the temperature dropped to −50 °C, the resin's plastic zone became substantially smaller. Even with higher fracture toughness, the tensile strain at break was still greatly reduced. In our previous studies [16,17] we examined how ply thickness and laminate design affect cryogenic CFRP performance at 77 K. It was found that thinner plies improve delamination resistance and shear strength by making fiber-matrix distribution more uniform and reducing resin pockets/fiber-rich zones [16]. Also, using thinner plies and better stacking helped to delay damage, especially where ply orientation causes interlaminar stress at cryogenics [17].

At RT, CFRP fatigue performance is improved with higher fiber modulus [18–21] and thinner plies [22,23]. Early studies looked at various fiber types and their effect on fatigue [18]. High-modulus fibers tended to resist further to onset of damage but fail more suddenly when cracks are formed, due to rapid energy release. High-tenacity fibers exhibit earlier but more gradually damage growth, since their strain at failure exceeded the matrix's fatigue limit [18]. Jones et al. [21] compared stress-life curves and found high-modulus fibers had better fatigue resistance due to different failure modes. Sihn et al. [22] and Amacher et al. [23] showed that thinner plies reduce microcracking, delamination, and splitting under static, fatigue, and impact loads. Katsivalis et al. [24] found that thin-ply CFRPs stayed impermeable to hydrogen even after being strained to 1.4 % at RT. These results indicate that thin plies and higher-modulus fibers can reduce microcrack formation, making them suitable for linerless low-pressure storage tanks.

Monitoring microcrack initiation in cryogenic environments still presents significant experimental challenges. The tests are complex, and early damage is often subtle. In previous studies [17,25], the authors proposed an in-situ method using an axial extensometer in liquid nitrogen (LN2); however, it only detected major damage level such as delamination, rather than early-stage microcracking. Furthermore, Li et al. [26] employed microfocus X-ray computed tomography to characterize cryogenic damage mechanisms in CFRP laminates, while Fujishiro et al. [27] used optical microscopy to investigate microscopic damage in crossply laminates at cryogenic temperature. These studies provide valuable insights into the initiation and evolution of damage under cryogenic conditions and complement the experimental challenges herein highlighted.

In the field of micromechanics, Camanho et al. [28] developed an in-situ strength theory based on Dvorak Law's [29] to predict 90° ply failure under different loads without complex testing or curve fitting. This model estimates ply strength using measurable engineering constants (e.g., interlaminar toughness, tensile and shear modulus), allowing prediction of fiber- and matrix-dominated failure modes. In parallel, several works have also shown that hydrostatic or constraint-type stresses strongly influence transverse crack initiation, particularly when matrix failure governs ply strength [30–33]. For instant, Parry and Wronski [30] demonstrated that applying superposed hydrostatic pressure to CFRP and glass fiber/epoxy composites increases the stress required for transverse failure, effectively delaying crack initiation by suppressing resin yielding. Following experimental works have reported that predictions from traditional yield criteria often do not match results when the resin is subjected to pure hydrostatic stress [32,33]. These limitations motivated the development of more advanced failure models, such as the LaRC03 criterion. While LaRC03 does not explicitly treat hydrostatic stress as a separate parameter, it incorporates the interaction of transverse tension and shear in a physically based manner. Importantly, it requires only standard material properties as input and has been applied successfully to predict transverse cracking in thin-ply laminates [34–39].

Moreover, we have to recognize that CTE mismatch generates residual stresses when cooling to cryogenic temperatures, which significantly affect transverse crack initiation. As reported by Pupurs et al. [39], in thin-ply laminates, the increase in transverse modulus of the 90° plies at low temperatures, combined with the decrease in transverse CTE, alters the stress distribution in the transverse plies and modifies the threshold for microcrack formation. García et al. [40] further demonstrated that these thermal residual stresses can reduce the mechanical load required for crack initiation. Although precise thermo-elastic properties at cryogenic temperatures are limited, the opposing effects of increased modulus and reduced CTE partially offset each other, and their net influence is inherently reflected in the measured engineering constants. Consequently, the LaRC03 model remains appropriate for predicting transverse crack initiation, as it incorporates these effects indirectly through the experimentally determined constants without explicitly modeling the residual stress field. Based on these characteristics, LaRC03 was selected in the present study to evaluate crack initiation under ambient and cryogenic conditions.

This study aims to fill existing gaps by investigating the influence of the carbon-fiber properties on the mechanical behavior and crack development of their respective CFRP composites at both RT and cryogenic temperatures. The investigation employs CFRP prepregs with varying fiber modulus and ply thickness design to assess their impact on the microcrack onset in both RT and 77 K conditions. Herein, material properties were measured and used to calculate the transverse strength of the 90° embedded ply in crossply laminates via the LaRC03 matrix failure criterion. By correlating these values with experimental performance, this work presents a novel approach to evaluate the effect of fiber modulus and ply thickness on crack development in thin-ply composites under cryogenic conditions. The objectives are threefold: (i) analyze the mechanical properties of various carbon-fiber composites with a cryogenic-design epoxy matrix tested at RT and 77 K, (ii) evaluate the LaRC03 criterion as a simpler alternative to in-situ methods for predicting transverse crack onset in cryogenic testing conditions, and (iii) examine how fiber modulus and ply thickness influence transverse cracking onset behavior at RT and 77 K. The findings offer valuable insights for the design and optimization of composite materials for applications in cryogenic environments.

2. Materials and methods

2.1. Prepreg material

For this study, a toughened epoxy resin designed for cryogenic environments and thin-ply prepregs, with curing temperature of 130 °C, was impregnated with three polyacrylonitrile (PAN)-based carbon fibers, maintaining a fiber areal weight of 70 g/m^2. Details on the epoxy resin can be found in Refs. [15–17]. The selected carbon fibers are summarized in Table 1, included the following commercial products: the intermediate-modulus (IM) HexTow® IMA (Hexcel Corporation, Salt Lake City, USA); the high-tenacity (HT) T700S and high-modulus (HM) M55J (Toray Industries, Roussillon, France).

The prepreg material was produced using a hot-melt impregnation unit from Roth Composite Machinery GmbH (Steffenberg, Germany). The continuous unidirectional prepreg tape was manufactured to achieve a fiber volume content (FVC) of 60 %. To attain a fiber areal weight of 70 g/m^2, a higher tow size (24 K) required increased pressure from the calendering system compared to lower tow sizes (12 K and 6 K). Despite achieving an average fiber areal weight of 70 g/m^2, 24 K fibers exhibited slightly less uniform distribution within the prepreg tape. This is attributed to the challenges in controlling fiber distribution when wider filament rovings undergo in-situ spreading. Nonetheless, thin-ply prepregs with high quality and homogeneity were successfully produced for this system. Fig. 1 displays a schematic representation of the prepreg process for each fiber type, along with representative samples of the prepreg tapes. All fibers presented in this study are supplied with epoxy-compatible sizing. Although variations in chemical composition and

Table 1
Main properties of the different carbon fibers utilized in this survey.

Commercial name	Referred CFRP name	Tensile modulus	Tensile strength	Tensile strain	Filament count	Rooving tex	Fiber diameter
-	-	*GPa*	*MPa*	*%*	-	*g/km*	*μm*
T700S	**HT Fiber**	230	4900	2.10	24 K	1650	≈7
IMA	**IM Fiber**	296	6067	1.90	12 K	446	≈5
M55J	**HM Fiber**	540	4020	0.80	6 K	218	≈5

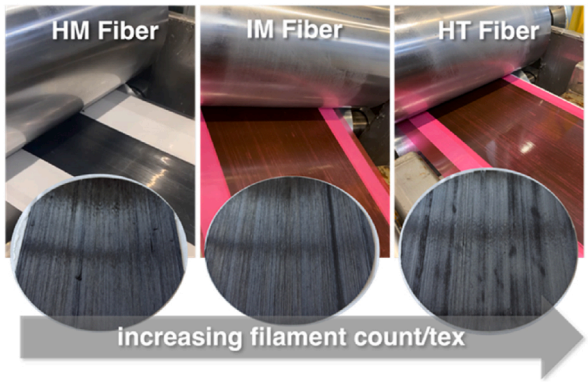

Fig. 1. Representative images of the thin-ply prepreg manufacturing for the different carbon-fiber systems.

concentration will influence composite properties, these effects were considered secondary and assumed to impact all systems in a comparable manner.

2.2. Composite laminates manufacturing

The composite laminates of the systems were hand-laid using the 70 g/m^2 prepreg tapes aforementioned. A summary of the manufactured laminates is displayed in Table 2. For obtaining the Energy Release Rate values of Mode I and Mode II, the laminates were manufactured for double cantilever beam (DCB) and end-notched flexure (ENF) test, respectively. The Tensile 0° and 90° laminates were manufactured as unidirectional (UD) of 1 and 2 mm thickness, while the In-Plane Shear laminates reached approximately 1.4 mm. To achieve varying ply thicknesses within the crossply composite laminates, the stacking sequence was designed as follows: $[0,90,\ 0,\ 90,90,\ 0,\ 90,90]_s$. This configuration ensured that 90° plies with thicknesses of 280 μm, 140 μm, and 70 μm were consistently constrained by adjacent 0° plies in a symmetrical format. This arrangement validated the differences in ply thicknesses, making them suitable for evaluation using the LaRC03 criterion. The final laminate thickness was of approximately 1.2 mm for all systems. All laminates were assembled manually, with evacuation steps implemented between layers to enhance layer cohesion and minimize porosity. Following assembly, the laminates were consolidated via autoclave processing. After consolidation, the laminates were inspected for defects using an ultrasound pool scanner, confirming the absence of significant porosity or uneven regions. Specimens were then precisely cut with a rotating blade cutting machine, ensuring smooth edges and minimal stress concentrations.

Thermogravimetric analysis (TGA) was conducted to determine the fiber volume content (FVC) following DIN 16459:2019–12 [41]. The average FVC of the laminates after curing was evaluated as 59 %, with the system HT Fiber exhibiting slightly greater deviations (±3 %) compared to HM Fiber (±1 %) and IM Fiber (±1 %). For further details on the equipment and methods aforementioned, please refer to Ref. [17].

2.3. Fracture toughness

Fracture toughness tests were conducted via energy release rate according to DIN EN ISO 6033 (Mode I) [42] and 6034 (Mode II) [43]. Mode I testing was conducted using double DCB specimens in a universal testing machine adapted for cryogenic conditions, with an initial crack length of 25 mm and measurements taken starting at 50 mm. Mode II tests were performed on specimens derived from the DCB samples as ENF using a 100 kN universal testing machine, also adapted for cryogenic testing. Both cryogenic tests were carried out in LN2 environments, ensuring specimens reached 77 K. At least four specimens were tested per system and temperature condition. For further descriptions of the experimental setup and procedures, please refer to Ref. [16]. The values of G_{Ic} were also calculated for use in the LaRC03 criterion instead of the average value of the R-curve (G_{IR}), avoiding the influence of fiber bridging and critical bending radius.

2.4. Tensile testing

Tensile testing was performed using a 100 kN universal testing machine adapted for cryogenic conditions (77 K, in-situ with LN2), from Franz Wohl + Partner Prüfmaschinen GmbH (Schalkau, Germany). A custom polytetrafluoroethylene (PTFE) mold, sealed with a silicone gasket, was designed for 1–2 mm thickness specimens to prevent LN2 leakage at the tabs-cavity. Testing followed ASTM D3039 [44] at RT environments, and similarly addapted to LN2 testing for cryogenic environments. An axial extensometer designed for LN2 operation measured local strain up to failure. For more details on the tensile testing setup, see Ref. [17]. In-plane shear tensile testing was also carried out according to ASTM D3518 [45] in both RT and 77 K, but here, the machine was equipped with strain gauge sensors to determine *x*- and

Table 2
Summary of testing methods and laminate configurations used to obtain the engineering constants required for the LaRC03 in-situ failure criterion.

Measurement	Standard	Stacking sequence	No. of layers	Laminate thickness	Constants[a]
Fracture Toughness Mode I	ISO 6033/ISO 15024	$[0]_{42}$	42	~3 mm	G_{Ic}, G_{IR}
Fracture Toughness Mode II	ISO 6034/ASTM 7905				G_{IIc}
Tensile 0°	ASTM D3039	$[0]_{14}$	14	~1 mm	E_{11}
Tensile 90°		$[0]_{28}$	28	~2 mm	E_{22}
Tensile Crossply[b]		$[0,90,0,90,90,0,90,90]_s$	16	~1.2 mm	–
In-Plane Shear ±45°	ASTM D3518	$[+45,-45]_{5s}$	20	~1.4 mm	G_{12}, ν_{12}, ν_{21}

[a] Here, G_{Ic} is the crack resistance onset, G_{IR} is the average R-curve fracture toughness mode I, and G_{IIc} is the fracture toughness mode II, respectively, E_{11} is the longitudinal modulus, E_{22} is the transversal modulus, G_{12} is the shear modulus, and ν_{12} and ν_{21} are the Poisson ratios in the *x*- and *y*-axis.

[b] Although ASTM D3039 does not specifically provide instructions for a tailored crossply laminate, the specimens followed a width of 25 mm, and for symmetry, 16 layers were used, resulting in an approx. Thickness of 1.2 mm.

y-strain values, allowing for the calculation of Poisson's ratios (ν_{12} and ν_{21}). These measurements were taken continuously up to laminate failure. The same PTFE container was utilized for maintaining the samples in LN2 throughout the test at 77 K.

2.5. Transverse crack onset analysis via optical microscopy

To assess crack onset behavior, a progressive stress-loading approach was adopted, where tensile specimens from each fiber system were subjected to increasing levels of applied tensile stress (as for Section 2.4). The resulting strain was recorded at each level, allowing comparison with the predicted failure strain values derived from the LaRC03 criterion. Since real-time in-situ crack monitoring is not feasible under cryogenic conditions, this qualitative 4 step-loading methodology was chosen to cover a wide range; from the initial predicted crack onset to near-final failure of the laminate (300, 450, 600, and 750 MPa at 296 K, and 275, 400, 525, and 650 MPa at 77 K). These values were chosen based on their ultimate tensile properties presented in Section 3.2. According to the LaRC03 criterion, transverse crack onset in thin embedded plies is defined as the instant formation of a crack through the thickness of the 90° ply. Experimentally, the transverse crack onset was defined as the appearance of a crack observable via microscope. Thus, embedded ply failure is given herein as a qualitative measure. At least 2 specimens of all systems were evaluated in microscopy after each level of load, in both testing environments. Table 1A in Appendix A summarizes the applied tensile stress and corresponding strain for each CFRP system at 296 K and 77 K. The purpose of Table 1A is to provide a global comparison of how each laminate responds to incremental stress levels in terms of strain across both testing temperatures for the qualitative analysis of crack onset.

3. Results and discussion

3.1. Fracture toughness

A comparison of the energy release rate Mode I of the three different fiber systems was carried out by plotting a representative average R-curves of each system at 296 K and 77 K, following the standard procedure in Ref. [42]. The R-curves shown in Fig. 2 were analyzed to identify the onset crack resistance G_{Ic} (at the first measured crack displacement of 50 mm), the evolution of resistance with crack displacement up to 100 mm, and the corresponding average values as G_{IR}. These parameters are relevant for the later application of the LaRC03 criterion, where the onset toughness is directly related to embedded ply failure.

At RT, crack propagation was stable for HT and IM Fiber specimens. Both exhibited higher onset toughness and increasing R-curves, with positive slopes indicating the activation of fiber bridging and crack-tip energy dissipation mechanisms. These mechanisms became more effective as the crack advanced and specimen compliance increased. Additionally, the smaller critical bending radius of HT and IM Fiber CFRP improved damage tolerance compared to HM. The larger fiber diameter of the HT Fiber specimens likely contributed to the highest G_{IR} values, as it increases fiber pull-out strength and promotes greater energy dissipation during crack growth, as mentioned by Chen et al. [46]. In contrast, the HM Fiber displayed partial stick–slip behavior, which is a common result of greater elastic energy release during crack growth. This behavior led to a flat R-curve with lower G_{IR} values, confirming its limited toughness despite the presence of a cryogenic-toughened epoxy matrix. In HM laminates, brittle fibers tend to fracture rather than contribute to bridging or pull-out, which suppresses toughening mechanisms.

At 77 K, all systems showed a marked change in fracture behavior compared to RT. Crack propagation shifted to a clear slip–stick mode, and the R-curves displayed negative slopes, indicating more elastic energy release and decreased in toughness as the crack advanced. This trend reflects the stiffening effect of temperature on the matrix and resulting suppression of the aforementioned toughening mechanisms. The plastic zone radius at the crack tip reduces significantly in cryogenic environments, as reported by Ref. [14], further limiting energy dissipation. The critical bending radius also increases as laminate modulus rises, further reducing the ability of fibers to open and bridge the crack. As a result, the overall potential for toughness decreases across all systems. These effects are consistent with earlier observations [9,16], where fracture surfaces at low temperature showed less resin debris and fiber pull-out, pointing to a brittle fracture mode. The mismatch in thermal expansion between fiber and matrix additionally amplifies local residual stresses, promoting earlier matrix cracking during propagation, as discussed by Ref. [3]. Shindo et al. [48–50] reported similar findings, noting that brittle matrix fracture at cryogenic conditions consumes much less energy than debonding or pull-out mechanisms. Among the systems, HM Fiber again exhibited the lowest G_{Ic} and G_{IR}. However, the

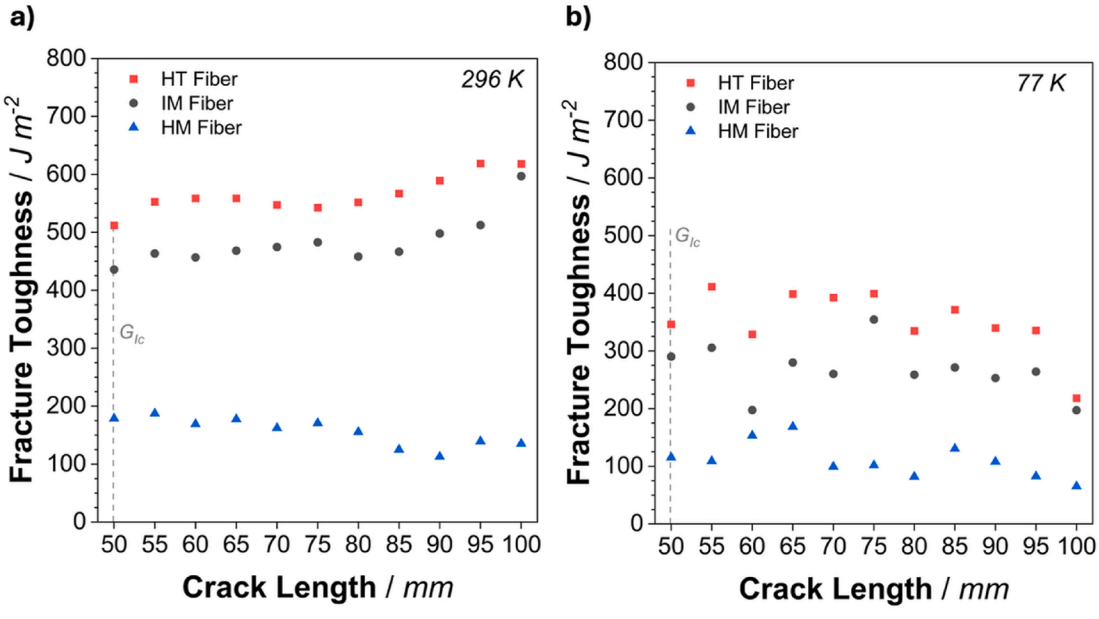

Fig. 2. Representative R-curves of the CFRP systems as fracture toughness Mode I at a) 296 K and b) 77 K testing.

relative loss was less pronounced, since its brittleness was already expressive at RT. In contrast, HT and IM Fiber laminates lost most of the benefits of fiber bridging and matrix plasticity, which explains the strong reduction in their R-curves, but still exhibited high values of G_{Ic} and G_{IR} compared to other literature values measuring energy release rate Mode I at 77 K [9], likely attributed to the ultra-tough resin designed for cryogenic environments.

Furthermore, Fig. 3 exhibits the force–displacement curves of representative specimens for the different systems in fracture toughness via energy release rate Mode II, at both 296 K and 77 K. At RT, HT and IM Fiber laminates exhibited ductile behavior with smooth crack propagation, indicating plastic deformation rather than direct shear failure. HM Fiber specimens showed a sharp failure onset, consistent with their brittle nature. Their Mode II fracture toughness values are comparable (77 K) or even lower than the Mode I values (RT). This suggests that, while both modes are influenced by the brittleness of HM fibers, the suppression of matrix shear yielding and plastic deformation affects G_{IIc} to a greater extent than G_{Ic}, leading to the observed behavior. The slope of the representative curves reflects the fiber modulus for each system: HM > IM > HT Fiber. It should be noted that specimen dimensions (width, thickness, and initial crack length) were highly consistent due to the use of an automatic wet-cutting machine and thin-plies, which minimizes variability in the ENF slopes. Further details on normalization of load-displacement curves can be seen in Oshima et al. [47].

At 77 K, all systems shifted towards a sharp shear failure. HT Fiber displayed a decrease in G_{IIc}, likely due to high deformation of the plies, resulting in a greater shear stress. IM Fiber showed a notable increase in value, suggesting an effective combination of fiber modulus and tenacity under cryogenic conditions. HM Fiber's G_{IIc} remained similar to RT, with only a minor reduction due to increased laminate brittleness. These trends highlight the combined influence of fiber modulus and ply deformation on shear resistance and the sensitivity of toughening mechanisms to temperature. The values of G_{Ic}, G_{IR}, and G_{IIc} for all fiber systems at both testing temperatures are summarized in Table 3 (Section 3.2).

3.2. Tensile properties of 0°, 90°, and ±45° laminates

Quasi-static tensile tests were performed on unidirectional 0°, 90°, and ±45° laminates at 296 K and 77 K to determine the engineering constants required for using the LaRC03 in-situ strength criterion. Relevant values for the criterion are summarized in Tables 3 and 4 for each respective environment. Additionally, Fig. 1A in Appendix A displays representative stress–strain curves for each system and testing method at both 296 K and 77 K testing, alongside the strength properties in Table A2 and Table 3A.

In the 0° configuration, tensile strength generally followed fiber modulus, with HT Fiber showing the highest failure strain and HM Fiber the lowest. At 77 K, all systems displayed reduced ductility, particularly HM Fiber, whose failure strain dropped to nearly half of the value measured at RT. Despite this, IM and HT Fiber specimens maintained relatively stable tensile strength across temperatures (≈2200–2400 MPa), reflecting the dominant role of the fibers in axial loading. In contrast, HM Fiber showed a pronounced decrease in both strength and failure strain, from 1708 MPa to 0.56 % at 296 K to 848 MPa and 0.31 % at 77 K, likely indicating greater sensitivity to low-temperature environments, leading to earlier failure.

For 90° laminates, failure strain increased with decreasing fiber modulus at 296 K. Here, the HT Fiber again showed the highest values. This trend aligns with higher G_{Ic} values seen in high-tenacity fibers. A general trend was observed between G_{IR} and 90° UD tensile failure strain, indicating that higher G_{IR} values corresponded to greater transverse strain capacity. This comparison was not extended to 77 K due to limitations in 90° UD tensile testing, where premature tab failure introduced significant variability in strain-to-failure across all systems. Nevertheless, the transverse elastic modulus values (E_{22}) remained consistent and were deemed suitable for use in the LaRC03 model.

In ±45° shear testing, the HT Fiber and IM Fiber laminates exhibited progressive damage behavior and higher axial strains at failure, whereas the HM Fiber showed early brittle failure and lower ductility. At 77 K, matrix stiffening led to increased shear modulus and ultimate stress in all systems. Notably, the HM Fiber, which was the most brittle at 296 K, showed a marked improvement in cryogenic shear performance, suggesting a temperature-induced shift in damage mechanisms and increased fiber–matrix cohesion.

3.3. Tensile behavior of crossply laminate

To evaluate the in-situ strength across different material systems and ply thicknesses, symmetric laminates were manufactured as described in Section 2.4, using 70 g/m^2 prepreg tapes to achieve nominal ply thicknesses of 280 μm, 140 μm, and 70 μm. These laminates were tested to

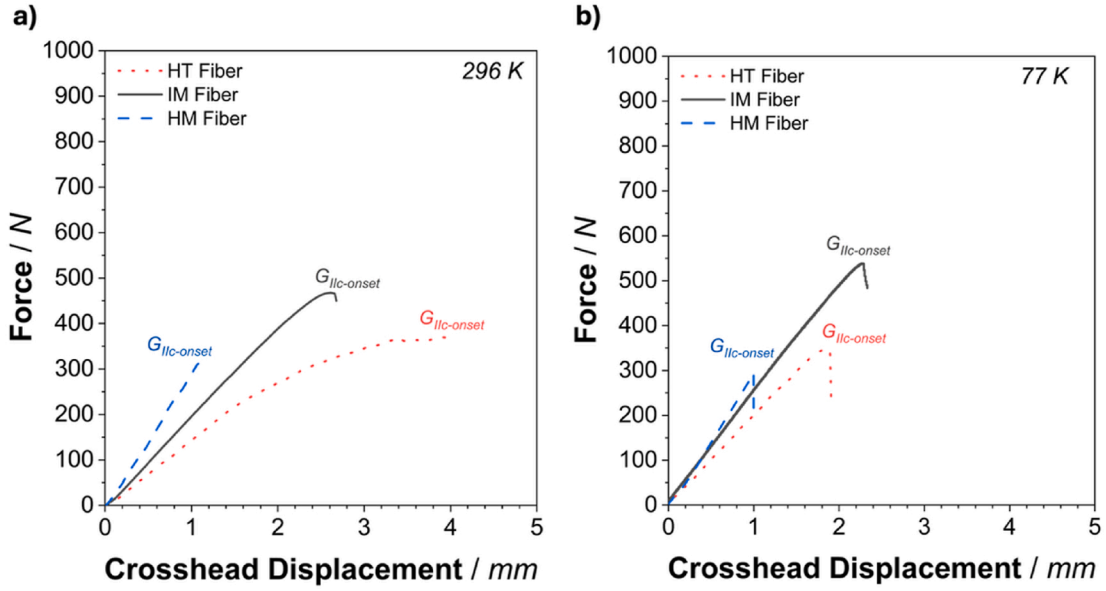

Fig. 3. Representative force–displacement behavior in energy release rate Mode II at a) 296 K and b) 77 K testing.

Table 3
Summary of relevant fracture toughness and tensile properties of all CFRP systems measured at 296 K.

CFRP System	G_{Ic} (J m^{-2})	G_{IR} (J m^{-2})	G_{IIc} (J m^{-2})	E_{11} (GPa)	E_{22} (GPa)	G_{12} (GPa)	ν_{12} (−)	ν_{21} (−)
HT Fiber	534 ± 12	553 ± 19	611 ± 50	124 ± 3	6.5 ± 0.4	5.0 ± 0.9	0.31	0.019
IM Fiber	432 ± 15	488 ± 17	688 ± 33	159 ± 5	6.9 ± 0.5	5.4 ± 0.1	0.29	0.013
HM Fiber	170 ± 18	145 ± 6	157 ± 53	305 ± 9	6.9 ± 0.4	6.2 ± 0.2	0.30	0.009

Table 4
Summary of relevant fracture toughness and tensile properties of all CFRP systems measured at 77 K.

CFRP System	G_{Ic} (J m^{-2})	G_{IR} (J m^{-2})	G_{IIc} (J m^{-2})	E_{11} (GPa)	E_{22} (GPa)	G_{12} (GPa)	ν_{12} (−)	ν_{21} (−)
HT Fiber	346 ± 21	320 ± 23	438 ± 79	137 ± 5	10.1 ± 0.1	7.3 ± 0.4	0.31	0.014
IM Fiber	290 ± 10	282 ± 21	733 ± 51	166 ± 3	10.9 ± 0.2	9.1 ± 0.3	0.29	0.012
HM Fiber	115 ± 15	101 ± 12	121 ± 9	308 ± 8	11.2 ± 0.2	11.2 ± 0.2	0.30	0.007

failure under both RT and cryogenic conditions. Representative stress–strain curves for each system are shown in Fig. 4a (296 K) and Fig. 4b (77 K).

At 296 K, the tensile modulus of the crossply laminates followed the fiber properties, with HT Fiber showing the highest strain-to-failure due to its higher tenacity, followed by IM Fiber, and HM Fiber exhibiting the lowest strain. The tough and ductile matrix (≈2.7 GPa elastic modulus at RT) limits full stress transfer to the fibers but allows a large plastic zone, smoothing out local stress concentrations and potential defects. At 77 K all systems showed an increase in modulus and a decrease in failure strain, with a slight reduction in ultimate stress. HM Fiber, being more brittle and higher-modulus, exhibited the largest drop in strength and failure strain, highlighting its sensitivity to embrittlement at cryogenic temperatures. HT and IM Fiber maintained relatively high strength, balancing modulus increase and reduced strain at failure. In crossply laminates, the failure strain of the matrix often limits the ultimate strength, a constraint that becomes more severe in cryogenic environments where matrix strain capacity is greatly reduced. As a result, fibers with high ultimate strength may not fully realize their potential, since matrix cracking initiates earlier and governs the laminate strength. A summary of the average properties is given in Table 5.

Table 5
Summary of average stress-strain properties of the crossply laminates at RT and 77 K.

Tensile properties of the crossply laminates at 296 K			
	HT Fiber	*IM Fiber*	*HM Fiber*
Stress at Failure (MPa)	896 ± 15	862 ± 22	612 ± 19
Strain at Failure (%)	1.49 ± 0.05	1.28 ± 0.02	0.56 ± 0.02
Young's Modulus (GPa)	59 ± 1	68 ± 3	126 ± 2
Tensile properties of the crossply laminates at 77 K			
	HT Fiber	*IM Fiber*	*HM Fiber*
Stress at Failure (MPa)	706 ± 55	789 ± 13	511 ± 50
Strain at Failure (%)	1.14 ± 0.12	0.98 ± 0.01	0.41 ± 0.01
Young's Modulus (GPa)	65 ± 3	77 ± 1	134 ± 1

3.4. LaRC03 criterion for in-situ strength of thin embedded plies

The in-situ strength prediction model developed at [28] was applied to assess the relationship between transverse failure and ply thickness for the composite systems in both 296 K and 77 K testing. The transverse stress to failure, Y_{is}^{T} in tension and S_{is}^{T} in shear are calculated with the engineering constants presented in Tables 3 and 4, and the ply thickness t.

$$Y_{is}^{T} = \sqrt{\frac{4\,G_{Ic}}{\pi\,t\left[\frac{1}{E_{22}} - \frac{\nu_{21}^{2}}{E_{11}}\right]}} \tag{1}$$

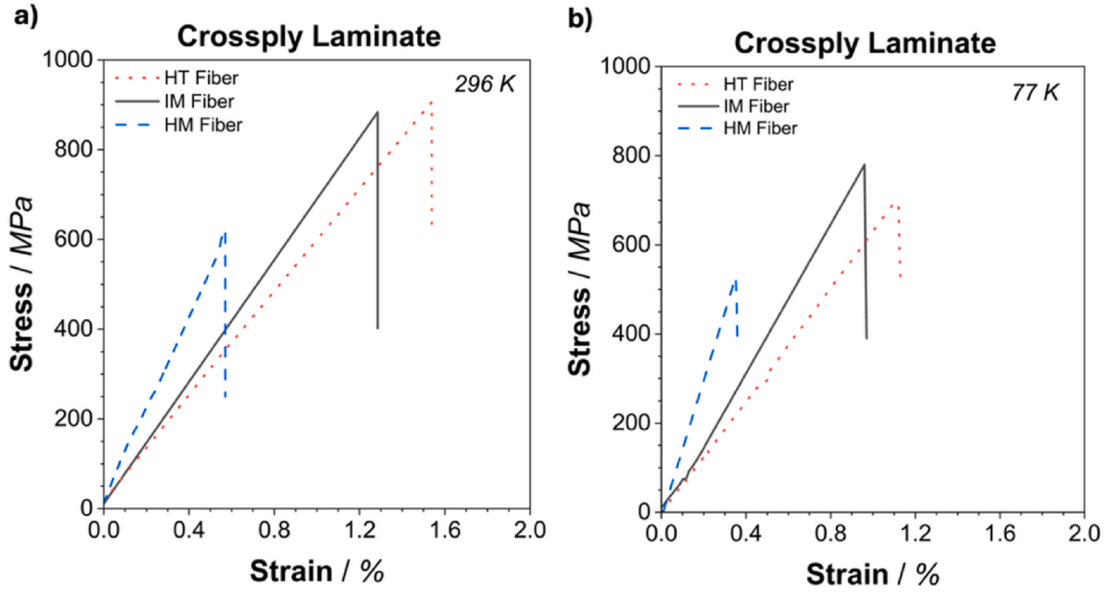

Fig. 4. Representative average tensile stress–strain curves of the crossply laminates tested at a) 296 K and b) 77 K.

$$S_{is}^{T} = \sqrt{\frac{8\, G_{IIc}\, G_{12}}{\pi\, t}} \tag{2}$$

To ensure the comparison aligned with the experimental results of this study, strain expressions for both Y_{is}^{T} and S_{is}^{T} were derived as outlined by Katsivalis et al. [51], as:

$$\varepsilon_{Y,is}^{T} = \frac{1}{E_{22}}\, Y_{is}^{T} \tag{3}$$

$$\varepsilon_{S,is}^{T} = \frac{S_{is}^{T}}{2\sqrt{2}} \tag{4}$$

The crossply laminates tested experimentally were laid from the 70 g/m^2 tapes, with 90° layer of varying ply thicknesses of 280 μm, 140 μm, and 70 μm within the same laminate, as mentioned in Table 2. The transverse strain to failure, in tension ($\varepsilon_{Y,is}^{T}$) and in shear ($\varepsilon_{S,is}^{T}$), as a function of ply thickness, for all CFRP systems in 296 K and 77 K are plotted in Fig. 5.

The performance of a crossply laminate is strongly influenced by the properties of its individual plies. For the in-situ transverse tensile strain, $\varepsilon_{Y,is}^{T}$, the most critical factors are G_{Ic} and the transverse modulus E_{22}. A higher 90° ply modulus increases the stored elastic energy in the embedded ply, thereby enhancing its in-situ strength. However, it simultaneously limits the matrix's capacity to elongate before crack initiation, thereby reducing the in-situ failure strain, $\varepsilon_{Y,is}^{T}$. In cryogenic environments, the embedded ply modulus E_{22} increases while G_{Ic} and matrix strain failure decreases, resulting in a lower $\varepsilon_{Y,is}^{T}$. Similarly, the $\varepsilon_{S,is}^{T}$ of a composite is generally higher than the former $\varepsilon_{Y,is}^{T}$, consistent with the typically larger G_{IIc} values and the higher strengths observed in ±45° shear testing compared to 90° UD tensile tests. At cryogenic temperatures, both in-situ tensile Y_{is}^{T} and S_{is}^{T} shear strength may increase slightly or significantly due to the elevated E_{22} and G_{12}. However, when expressed in terms of failure strain $\varepsilon_{Y,is}^{T}$ and $\varepsilon_{S,is}^{T}$, they can also exhibit

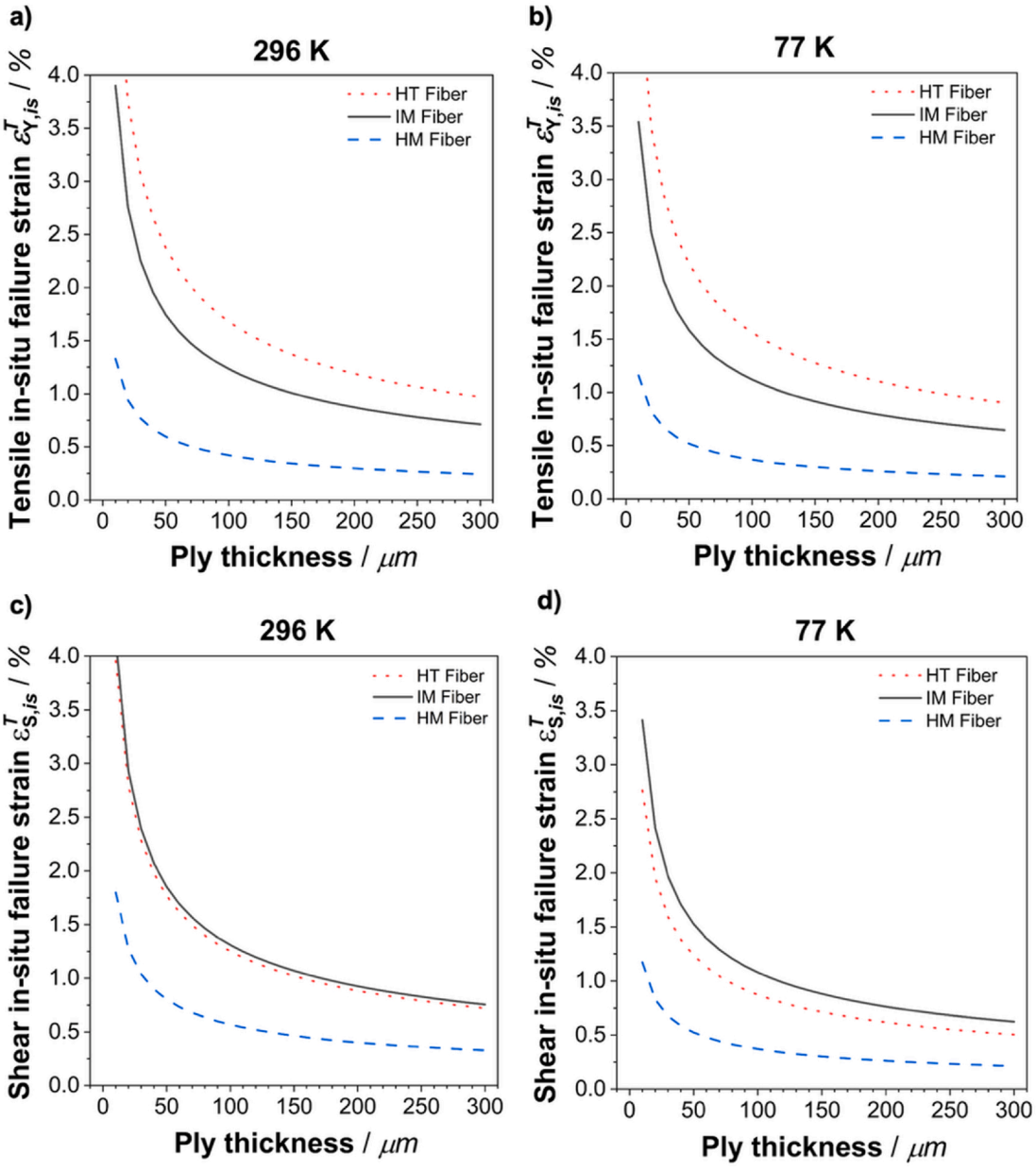

Fig. 5. Transverse in-situ 90° embedded ply failure strain as a function of ply thickness for the different composite systems calculated from the LaRC03 model: a) 296 K tensile, b) 77 K tensile, c) 296 K shear, and d) 77 K shear.

slightly decrease from 296 K to 77 K when G_{IIc} is affected negatively.

The curves in Fig. 5 show that the in-situ tensile failure strain $\varepsilon^{T}_{Y,is}$ and in-situ shear failure strain $\varepsilon^{T}_{S,is}$ of IM laminates were very similar, both decreasing by approximately 10 % when transitioning from 296 K to 77 K. The IM Fibers offered the best combined values of G_{Ic}, G_{IIc}, E_{22}, and G_{12}, enabling the material to effectively resist both tensile- and shear-induced microcracking. HT Fiber exhibited the highest $\varepsilon^{T}_{Y,is}$, primarily due to its superior G_{Ic}, which delays tensile crack initiation. However, its lower neighboring ply modulus E_{11} made it more susceptible to shear-driven damage, resulting in comparatively limited $\varepsilon^{T}_{S,is}$ values—slightly lower than those of IM Fiber. In contrast, the HM Fiber system showed comparable or even higher in-situ strength than HT Fiber, but with significantly lower in-situ failure strain values. The reduced G_{Ic} and G_{IIc} limit overall transverse crack resistance, and although the high modulus neighboring plies can help suppress elongation in the embedded ply, the drastic reduction in failure strain is more relevant.

The $\varepsilon^{T}_{Y,is}$ failure strain curve exhibited a rather gradient increase by decreasing ply thickness below 50 μm, beyond which the values transitioned quickly toward infinity, indicating an increasing size effect. HM Fiber, on the other hand, exhibited a near-plateau in $\varepsilon^{T}_{Y,is}$ values down to 50 μm, followed by a sharp increase, indicating a less pronounced benefit from thin-ply configurations. For $\varepsilon^{T}_{S,is}$, the transition is more gradual across all CFRP systems but still shows a consistent increase in strain capacity below the same 50 μm ply thickness threshold.

3.5. Evaluation of Larc03 criterion for failure strain of embedded plies at 296 K and 77 K

The experimental evaluation of crack initiation was compared with the predictions from the LaRC03 model. The same crossply tensile specimens used and characterized in Fig. 5 were employed for this analysis. In the analysis, the comparison between experimental observations and the LaRC03 predictions was performed using strain curves instead of a categorical classification. Specifically, the transverse cracking strains $\varepsilon^{T}_{Y,is}$ and shear cracking strains $\varepsilon^{T}_{S,is}$ were plotted as functions of ply thickness alongside the applied load level in four stages, for the three different ply thicknesses studied of each CFRP material. Each combination of ply thickness and applied load defines a "crosspoint" on these curves. At each crosspoint, the microscopy observations were compared with the model predictions:

Crosspoints below the LaRC03 failure strains ($\varepsilon^{T}_{Y,is}$ or $\varepsilon^{T}_{S,is}$):

The model predicts that no cracks should be seen here. If cracks are experimentally observed, then the model is non-conservative (failure occurs earlier than predicted). If no cracks are observed, the model agrees with the experiment.

Crosspoints above the LaRC03 failure strains ($\varepsilon^{T}_{Y,is}$ or $\varepsilon^{T}_{S,is}$):

The model predicts that cracking should occur. If cracks are experimentally observed, then the model agrees. If no cracks are observed, then the model is conservative (failure is delayed compared to the prediction).

To illustrate this comparison, microscopy images of the observed cracks are shown alongside the strain–thickness–load plots. This provides a direct visual link between the predicted crack onset and the experimentally observed damage.

3.5.1. HT Fiber

The experimental results vs. the LaRC03 model predictions for the HT Fiber system at 296 K are summarized in Fig. 6. As discussed previously, the high-tenacity fiber provides the composite with significant global elongation potential and toughness. This increases the tensile strength of the ply but also raises shear stresses from neighboring plies, thereby reducing the in-situ shear strength. In Fig. 6, it is observed that at 600 MPa (1.03 % strain), transverse cracks appear in the 280 μm plies, in agreement with the in-situ failure limits predicted by the criterion. When the load is further increased to 750 MPa (1.29 % strain), cracks are also observed in the 140 μm plies, again consistent with the predicted shear-driven failure $\varepsilon^{T}_{S,is}$. Furthermore, the microscopy images also display signs of shear-delamination longitudinal to the 0° neighboring plies, strengthening the idea that shear stress is highly promoted in this high-tenacity laminate. Overall, the HT Fiber crossply laminate exhibits 90° ply failure within the strain range defined by the LaRC03 model, confirming good alignment between experimental results and model predictions at RT testing conditions. No clear "crosspoint" above the failure prediction lines was found without a crack.

Fig. 7 presents the summarized values of the HT Fiber specimen at 77 K. Compared to 296 K, transverse cracks were observed more frequently, yet the overall damage appeared less severe. The crack onset levels were observed as follows: At 525 MPa (0.80 % strain), the first cracks were detected in the 280 μm ply, with additional cracks appearing in the 140 μm ply at 650 MPa (0.92 % strain). No cracking was observed in the 70 μm ply at any load level. In this case, the LaRC03

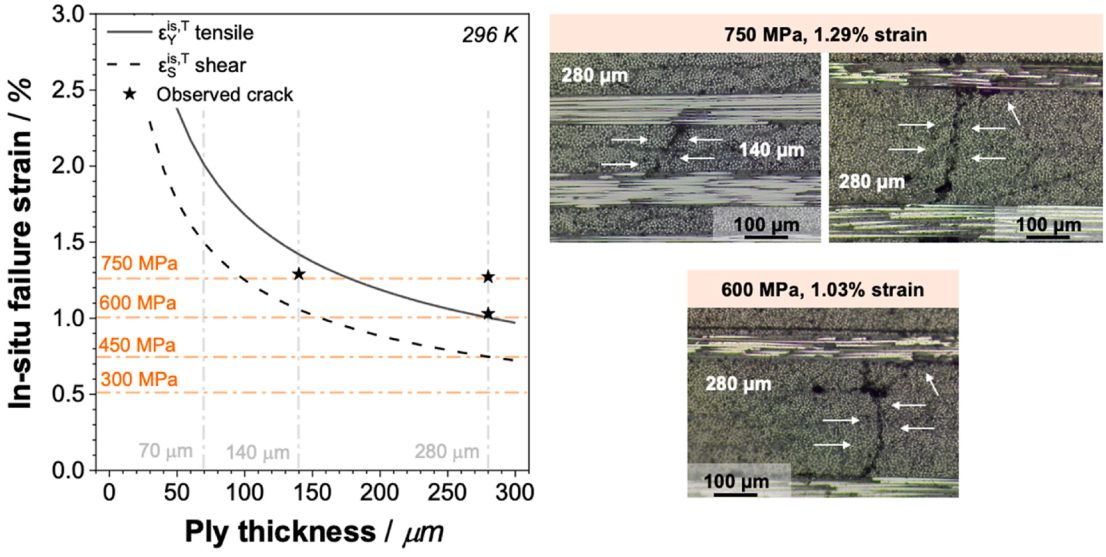

Fig. 6. Comparison of HT Fiber crossply laminates predicted crack initiation strains from the LaRC03 criterion with experimentally observed cracking for different ply thicknesses and load levels at RT testing.

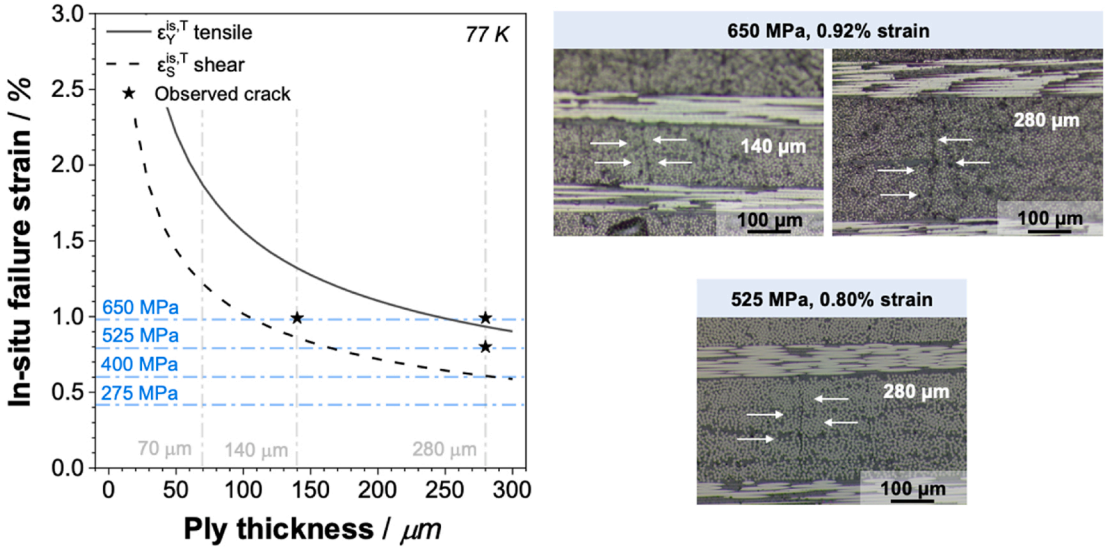

Fig. 7. Comparison of HT Fiber crossply laminates predicted crack initiation strains from the LaRC03 criterion with experimentally observed cracking for different ply thicknesses and load levels at cryogenic testing.

criterion shifted toward a more conservative prediction, underestimating the actual microcracking within the laminate. This trend may be attributed to the combined effects of cryogenic temperature on the material behavior: while the high-tenacity fiber permits significantly more elongation and thus shear at RT, this effect is reduced at 77 K due to stiffening of the plies. However, the resulting decrease in matrix ductility decreases the extent of the fracture process zone, while the elevated modulus concentrates stress more effectively between tensile and shear. This shift in the deformation mechanism may suppress the earlier onset of shear-driven failure observed at RT, and thus might not be fully captured by the model. There were no cases where the model predicted failure earlier than the actual observed crack initiation.

3.5.2. IM Fiber

For the IM Fiber composite at 296 K, Fig. 8 summarizes the experimental and LaRC03 model comparison and displays the relevant microscopy images of the embedded plies. According to the model, the first transverse cracks were expected to initiate at 0.75 % strain in the 280 µm ply. However, no cracks were observed experimentally up to 0.83 %, indicating that the model was conservative up to this point. When increasing the load to 750 MPa (1.10 % strain), transverse cracks were observed in the 280 µm ply, consistent with the model's predictions. At this stress-strain level, the model also anticipated cracking in the 140 µm ply, although they were not found in the microcopy analysis. Overall, the LaRC03 model showed a conservative tendency for the IM Fiber system at RT, predicting crack onset slightly earlier than it occurred in practice (e.g. as the "crosspoints" at 750 MPa with 140 µm, and 600 MPa at 280 µm).

The same correlation was carried out at 77 K, as displayed by Fig. 9. Here, no visible transverse cracks were detected up to 525 MPa, corresponding to a strain of 0.71 %. Even though the LaRC03 model predicted crack initiation in the 280 µm ply by this point. This again indicates that the model was conservative at this load level. However, a good agreement between model and experiment was observed when the load was increased to 650 MPa (0.84 % strain), where transverse cracks in the 280 µm ply were consistently detected across all specimens. Compared to RT, the LaRC03 model showed improved accuracy under cryogenic conditions, transitioning from conservative to closely predictive

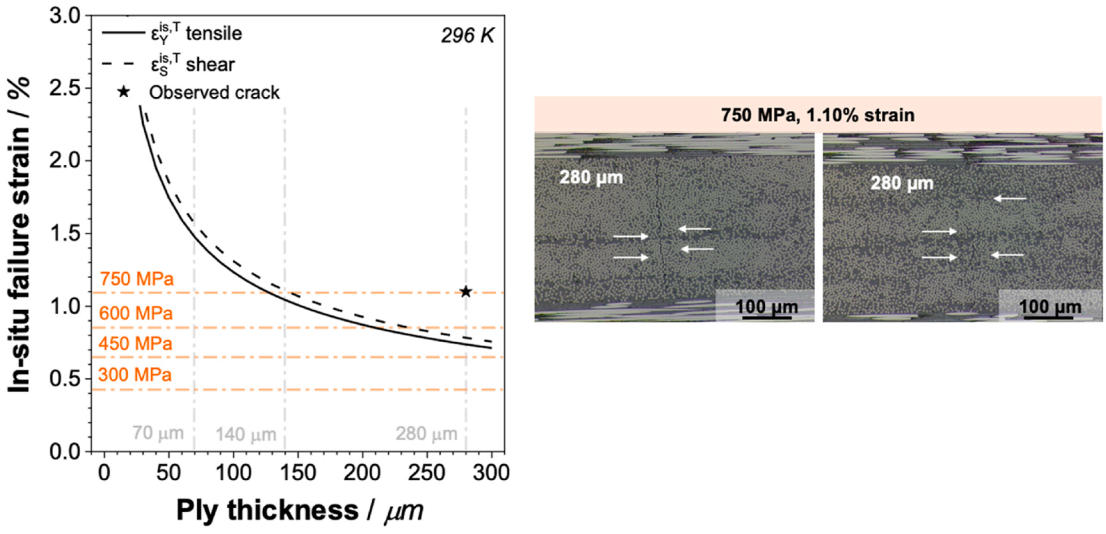

Fig. 8. Comparison of IM Fiber crossply laminates predicted crack initiation strains from the LaRC03 criterion with experimentally observed cracking for different ply thicknesses and load levels at RT testing.

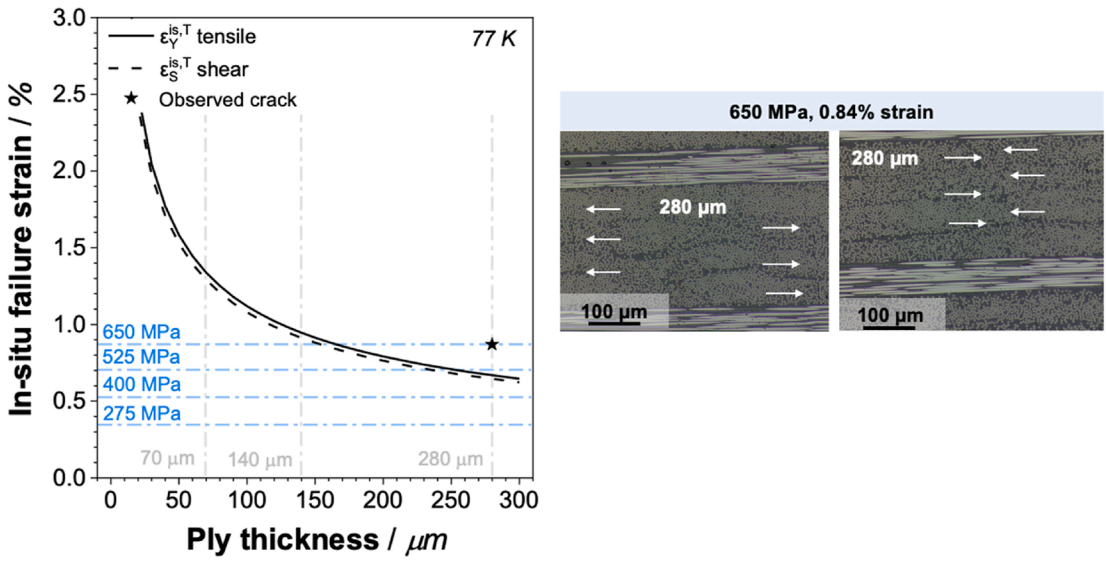

Fig. 9. Comparison of IM Fiber crossply laminates predicted crack initiation strains from the LaRC03 criterion with experimentally observed cracking for different ply thicknesses and load levels at cryogenic testing.

behavior. This improved match may suggest that the unusual ultra-toughened matrix at RT leads to deviation from model predictions. Eventually, the increase in matrix modulus and linear elastic regime at cryogenic temperatures shifts the behavior toward the assumptions underlying the LaRC03 criterion, improving its predictive accuracy.

3.5.3. HM Fiber

The model and experimental comparison values measured at 296 K are summarized in Fig. 10. As expected for a composite reinforced with high-modulus fibers, both $\varepsilon^{T}_{Y,is}$ and $\varepsilon^{T}_{S,is}$ were significantly lower than in the other systems. At the initial load level of 300 MPa (0.27 % strain), the model predicted transverse cracks in the 280 µm ply, whereas none were observed experimentally, indicating that the model is conservative. This discrepancy may be attributed to an extended fracture process zone at RT, where the matrix retains sufficient plasticity to locally delay crack propagation. However, as the applied stress increased to 450 MPa (0.41 % strain) and 600 MPa (0.55 % strain), the model predictions matched closely with the experimental onset of damage. Notably, HM Fiber was the only system in which transverse cracks appeared even in the thinnest 75 µm ply.

At 600 MPa, the crossply laminate was nearing its structural limit; cracks were present in all plies and, in some regions, were nearly interconnected. Optical microscopy revealed clear signs of extensive damage and delamination, suggesting imminent global failure. The angled appearance of some cracks indicates localized ply detachment and the onset of full delamination, consistent with the advanced failure stage observed in Fig. 10. This behavior reflects the fracture mechanics typical of high modulus systems: the higher modulus neighboring plies limits elongation and plastic deformation, thus reducing the energy absorption capacity of the system.

The same comparison of the HM Fiber system tested at cryogenic temperature is summarized in Fig. 11. At 225 MPa and 0.19 % strain, no transverse cracks were observed, aligning with the LaRC03 model. Here, cracks initiated in the 280 µm and 140 µm plies at 350 MPa (0.29 % strain), and in all ply thicknesses by 475 MPa (0.37 % strain), with microscopy revealing dense cracking and early shear in thinner

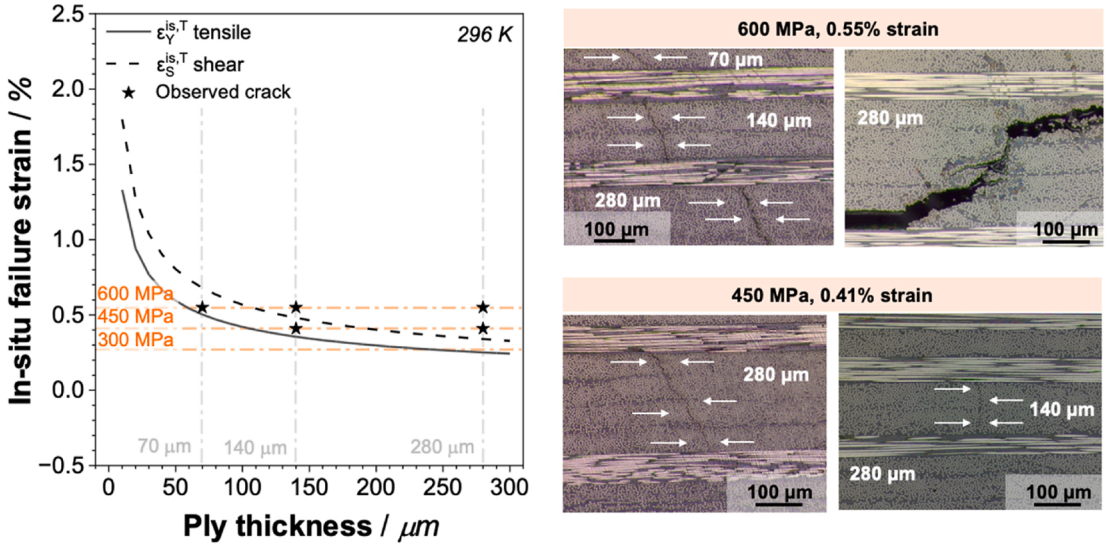

Fig. 10. Comparison of HM Fiber crossply laminates predicted crack initiation strains from the LaRC03 criterion with experimentally observed cracking for different ply thicknesses and load levels at RT testing.

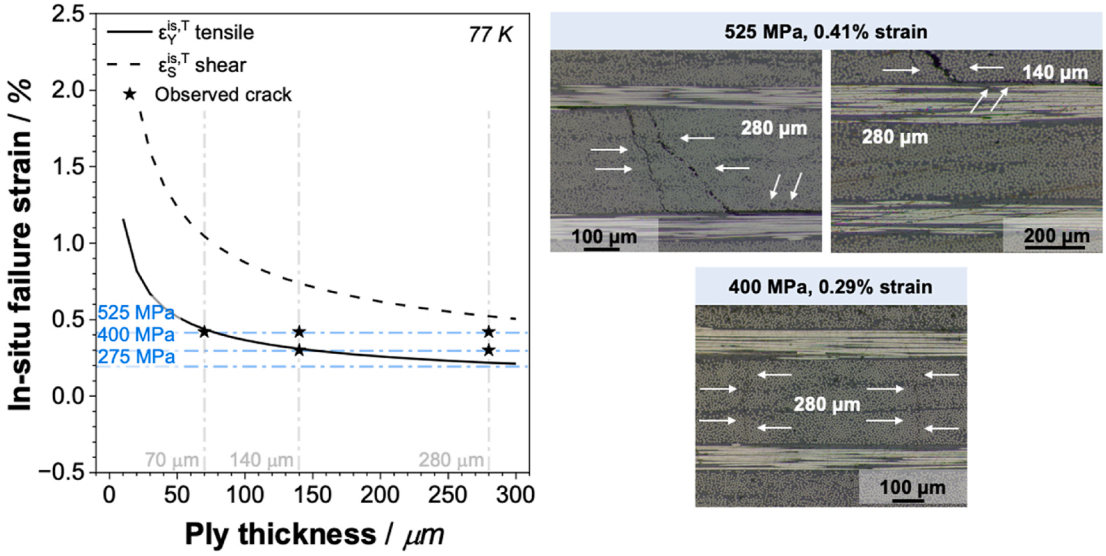

Fig. 11. Comparison of HM Fiber crossply laminates predicted crack initiation strains from the LaRC03 criterion with experimentally observed cracking for different ply thicknesses and load levels at cryogenic testing.

plies—closely aligning with LaRC03 predictions and indicating imminent failure. This supports the view that the ultra-tough resin effectively performs at 77 K by maintaining some extent of toughness. Thus, aligning the composite's behavior more closely with the assumptions of the model. The initially difference between $\varepsilon_{Y,is}^{T}$ and $\varepsilon_{S,is}^{T}$ failure strain observed at RT is reduced at 77 K. As a result, the balance of stress distribution across tensile and shear modes shifts, leading to more simultaneous failure mechanisms, especially in thinner plies. The measured average tensile strength of the HM Fiber crossply laminate at 77 K was 511 MPa at 0.41 % strain, alongside the ultimate failure of the composite (see Table 5). Some specimens even failed before reaching the next load level.

4. Conclusion

The present study focused on evaluating the mechanical behavior and onset of transverse microcracking in thin-ply CFRP laminates with different fibers at ambient and cryogenic conditions, using the LaRC03 failure criterion. The main conclusions are as follows.

Mechanical properties at 296 K and 77 K: Fracture toughness tests showed that IM fibers provided the best balance between Mode I and Mode II toughness. HM fibers exhibited significantly lower values and increased brittleness, while HT fibers reached the highest G_{Ic} and G_{IR} values, but with reduced G_{IIc} compared to IM fibers. IM and HT systems showed rising toughness during crack propagation, indicating fiber bridging, whereas HM systems maintained a flat R-curve. At 77 K, G_{Ic} decreased in all systems while G_{IIc} remained similar, and all specimens displayed stick–slip behavior with a negative R-curve slope, reflecting reduced toughening mechanisms. Tensile tests 0° UD showed reduced ductility at 77 K, most severely for HM Fibers whose failure strain fell to nearly half the RT value. Matrix stiffening at 77 K increased shear modulus and ultimate stress, with ±45° laminates showing notable G_{12} increase due to enhanced fiber–matrix cohesion. For 90° laminates, failure strain increased with decreasing fiber modulus, correlating with higher G_{Ic} values and greater transverse strain capacity.

Evaluation of crack onset on embedded plies via LaRC03: HT fibers exhibited the highest in-situ transverse failure strain $\varepsilon_{Y,is}^{T}$ at both RT and 77 K, consistent with higher G_{Ic} values. Cracks were detected at 280 μm and 140 μm plies, but not in 70 μm plies. At RT, cracks appeared at 280 μm (600 MPa) and 140 μm (750 MPa), while at 77 K they initiated earlier at 280 μm (525 MPa) and 140 μm (650 MPa). At 77 K, $\varepsilon_{S,is}^{T}$ decreased due to reduced G_{IIc}, increasing susceptibility to shear-driven failure. LaRC03 predictions matched well, with a slightly conservative tendency.

IM fibers showed slightly lower $\varepsilon_{Y,is}^{T}$ but maintained a favorable balance with $\varepsilon_{S,is}^{T}$. Thin-ply benefits were evident, with no cracks in 70 μm or 140 μm plies, and failure limited to 280 μm plies near ultimate stress (750 MPa at RT, 650 MPa at 77 K). Predictions were conservative, with failures only in the thickest ply. HM fibers displayed the lowest $\varepsilon_{Y,is}^{T}$ and $\varepsilon_{S,is}^{T}$, consistent with low G_{Ic} and G_{IIc}. Cracks were observed across all ply thicknesses: at RT, 140 μm plies failed at 450 MPa and 70 μm at 600 MPa; at 77 K, failures occurred at 400 MPa (140 μm) and 525 MPa (70 μm). Matrix stiffening improved shear performance, but transverse failure remained severe. Predictions aligned closely, reflecting the brittle character of the system. The four experimental loading steps were consider sufficient for a qualitative assessment of microcrack onset. While additional steps would enhance resolution for quantitative model validation, such refinement was beyond the scope of the present work.

Overall: IM Fibers demonstrated the best performance against cryogenic transverse microcracking, offering a favorable balance between plastic and elastic energy. The LaRC03 criterion showed good agreement with experimental results, providing valuable support for material design where in-situ methods are still limited under cryogenic conditions. While HM Fiber performed worse in quasi-static measurements, it is expected that their potential benefits observed here could translate to fatigue performance, suggesting a natural next step for further studies. These findings contribute to the design of CFRP laminates for linerless cryogenic storage tanks by providing relevant engineering constants for different carbon fiber types, highlighting important correlations, and offering a more accessible alternative to complex in-situ testing.

CRediT authorship contribution statement

Eduardo Szpoganicz: Writing – review & editing, Writing – original draft, Visualization, Methodology, Investigation, Formal analysis, Data curation, Conceptualization. **Fabian Hübner:** Writing – review & editing, Validation, Supervision, Conceptualization. **Uwe Beier:** Writing – review & editing, Validation, Supervision. **Edgard Boutant:** Investigation, Formal analysis. **Holger Ruckdäschel:** Writing – review & editing, Validation, Supervision, Project administration, Funding acquisition.

Declaration of competing interest

The authors declare that they have no known competing financial interests or personal relationships that could have appeared to influence the work reported in this paper.

Acknowledgement

This project was carried out under the guidance of Industrieanlagen-Betriebsgesellschaft mbH (IABG) and financed by the Bavarian Ministry of Economic Affairs, Regional Development and Energy (STmWi) according to the registration number BLU-2109-0024. Furthermore, to Lukas Endner (University of Bayreuth) for his support on sample preparation for optical microscopy

Appendix A

The representative average stress–strain curves for each laminate system and testing method at both 296 K and 77 K discussed in Section 3.2, is presented in Fig. A1.

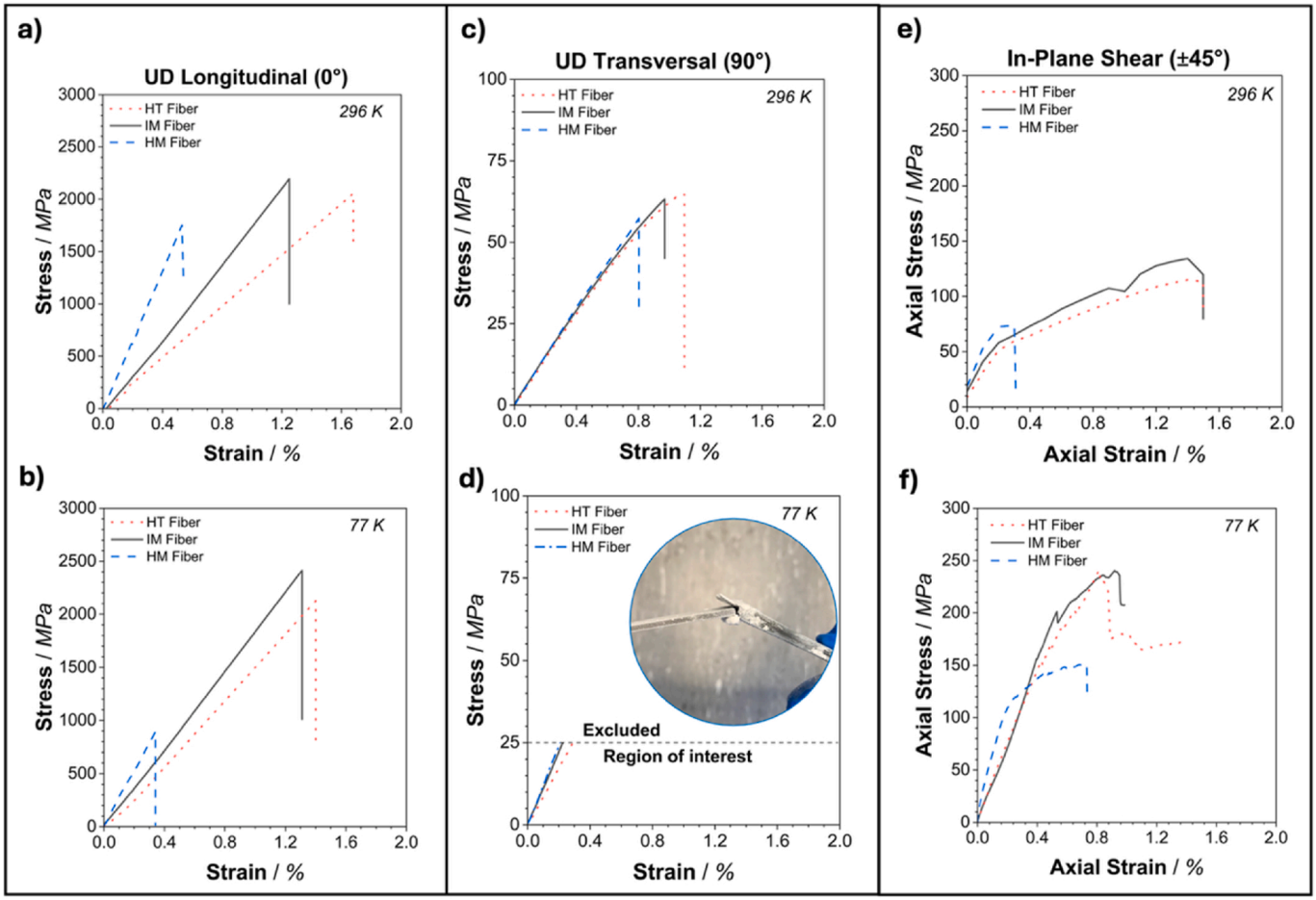

Fig. 1A. Representative average stress-strain curves of tensile testing for the different composite systems as UD longitudinal 0° a) at 296 K and b) at 77K, UD transversal 90° c) at 296 K and d) at 77 K, in-plane shear ±45° laminates e) at 296 K and f) 77 K.

Table 1A
Applied tensile load stress and the corresponding strain of each CFRP system at both 296 K and 77 K.

Applied Stress	HT Fiber	IM Fiber	HM Fiber	HT Fiber	IM Fiber	HM Fiber
(MPa)	*Resulting strain (%) at 296 K*			*Resulting strain (%) at 77 K*		
275	–	–	–	0.42	0.35	0.19
300	0.51	0.42	0.27	–	–	–
400	–	–	–	0.61	0.52	0.29
450	0.76	0.65	0.41	–	–	–
525	–	–	–	0.80	0.70	0.37
600	1.03	0.83	0.55	–	–	–
650	–	–	–	0.99	0.88	-*
750	1.29	1.10	-*			

* Specimens failed before reaching this level of applied tensile load.

Table 2A
Summary of tensile properties of all CFRP systems measured at 296 K.

CFRP System	0° Laminate		90° Laminate		±45° Laminate	
	Strength (MPa)	Failure Strain (%)	Strength (MPa)	Failure Strain (%)	Axial Strength (MPa)	Axial Failure Strain (%)
HT Fiber	2205 ± 66	1.67 ± 0.06	75 ± 23	1.12 ± 0.13	125 ± 21	1.52 ± 0.12
IM Fiber	2178 ± 38	1.23 ± 0.03	69 ± 18	1.02 ± 0.10	133 ± 30	1.48 ± 0.05
HM Fiber	1708 ± 37	0.59 ± 0.06	56 ± 24	0.84 ± 0.09	82 ± 12	0.38 ± 0.09

Table 3A
Summary of tensile properties of all CFRP systems measured at 77 K.

CFRP System	0° Laminate		90° Laminate		±45° Laminate	
	Strength (MPa)	Failure Strain (%)	Strength (MPa)	Failure Strain (%)	Axial Strength (MPa)	Axial Failure Strain (%)
HT Fiber	2449 ± 92	1.39 ± 0.05	*	*	257 ± 41	0.87 ± 0.15
IM Fiber	2407 ± 171	1.16 ± 0.05	*	*	244 ± 17	0.76 ± 0.08
HM Fiber	848 ± 63	0.31 ± 0.03	*	*	131 ± 29	0.65 ± 0.14

* Values could not be determined as failure occurred prematurely in the tab area for all systems.

Data availability

Data will be made available upon request.

References

[1] S. Tiwari, M. Pekris, J. Doherty, A review of liquid hydrogen aircraft and propulsion technologies, Int. J. Hydrogen Energy 57 (2024) 1174–1196.
[2] J. Hwang, K. Maharjan, H. Cho, A review of hydrogen utilization in power generation and transportation sectors: achievements and future challenges, Int. J. Hydrogen Energy 48 (2023) 28629–28648.
[3] A. Air, M. Shamsuddoha, B.G. Prusty, A review of type V composite pressure vessels and automated fibre placement based manufacturing, Composer Part B 253 (2023) 110573.
[4] N. Liu, B. Ma, F. Liu, W. Huang, B. Xu, L. Qu, Y. Yang, Progress in research on composite cryogenic propellant tank for large aerospace vehicles, Composer Part A Appl Sci Manuf 143 (2021) 106297.
[5] Z. Sápi, R. Butler, Properties of cryogenic and low temperature composite materials – a review, Cryogenics 111 (2020) 103190.
[6] J. Hohe, A. Neubrand, S. Fliegener, C. Beckmann, M. Schober, K. Weiss, S. Appel, Performance of fiber reinforced materials under cryogenic conditions—A review, Compos. Appl. Sci. Manuf. 141 (2021) 106226.
[7] J.F. Timmerman, M.S. Tillman, B.S. Hayes, J.C. Seferis, Matrix and fiber infuences on the cryogenic microcracking of carbon fiber/epoxy composites, Composites Part A 33 (2002) 323–329.
[8] J. Timmerman, B. Hayes, J. Seferis, Cryogenic microcracking of carbon Fiber/Epoxy composites: influences of fiber-matrix adhesion, J. Compos. Mater. 37 (2003) 1939–1950.
[9] W.S. Johnson, M.M. Pavlick, M.S. Oliver, Determination of interlaminar toughness of IM7/977-2 composites at temperature extremes and different thicknesses, NASA Reports (2005).
[10] J. Hohe, M. Schober, S. Fliegener, K. Weiss, S. Appel, Effect of cryogenic environments on failure of carbon fiber reinforced composites, Compos. Sci. Technol. 212 (2021) 108850.
[11] J. Hohe, M. Schober, K. Weiss, S. Appel, Validation of Puck's failure criterion for CFRP composites in the cryogenic regime, CEAS Space Journal 13 (2020) 145–153.
[12] W. Wei, H. Rongjin, H. Chuanjun, Y. Zhao, S. Li, L. Laifeng, Cryogenic performances of T700 and T800 carbon fibre- epoxy laminates, IOP Conf. Ser. Mater. Sci. Eng. 102 (2015) 012016.
[13] Y. Li, J. Meng, J. Luo, P. Wang, J. Ma, Z. Zhao, H. Lei, Cryogenic mechanics and damage behaviors of carbon fiber reinforced polymer composites, Compos. Appl. Sci. Manuf. 169 (2023) 107484.
[14] F. Hübner, A. Brückner, T. Dickhut, V. Altstädt, A. Rios de Anda, H. Ruckdäschel, Low temperature fatigue crack propagation in toughened epoxy resins aimed for filament winding of type V composite pressure vessels, Polym. Test. 102 (2021) 107323.
[15] F. Hübner, M. Hoffmann, N. Sommer, V. Altstädt, A. Scherer, T. Dickhut, H. Ruckdäschel, Temperature-dependent fracture behavior of towpreg epoxy resins for cryogenic liquid hydrogen composite vessels: the influence of polysiloxane toughenens on the resin yield behavior, Polym. Test. 113 (2022) 107678.
[16] E. Szpoganicz, F. Hübner, U. Beier, M. Geistbeck, H. Ruckdäschel, The effect of prepreg ply thickness in carbon fiber reinforced composites on intralaminar toughness and shear strength in cryogenic environments for liquid hydrogen storage tanks, Compos. B Eng. 292 (2025) 112077.
[17] E. Szpoganicz, F. Hübner, U. Beier, M. Geistbeck, M. Korff, L. Chen, Y. Tang, T. Dickhut, H. Ruckdäschel, Effect of prepreg ply thickness and orientation on tensile properties and damage onset in carbon-fiber composites for cryogenic environments, Compos. Struct. 359 (2025) 118996.
[18] O. Konur, F.L. Matthews, Effect of the properties of the constituents on the fatigue performance of composites: a review, Composites 20 (4) (1989) 277–289.
[19] P.T. Curtis, B.B. Moore, A comparison of plain and double waisted coupons for static and fatigue tensile testing of unidirectional GRP and CFRP, in: I.H. Marshall (Ed.), Composite Structures, vol. 2, Applied Science Publishers Ltd, 1983.
[20] R. Guo, C. Li, Y. Niu, G. Xian, The fatigue performances of carbon fiber reinforced polymer composites – a review, J. Mater. Res. Technol. 21 (2022) 4773–4789.
[21] C.J. Jones, R.F. Dickson, T. Adam, H. Reiter, B. Harris, The environmental fatigue behaviour of reinforced plastics, Proc. Roy. Soc. Lond. A 396 (1984) 315–338.
[22] S. Sihn, R. Kim, K. Kawabe, S. Tsai, Experimental studies of thin-ply laminated composites, Compos. Sci. Technol. 67 (2007) 996–1008.
[23] R. Amacher, J. Cugnoni, J. Botsis, Thin ply composites: experimental characterization and modeling, Compos. Sci. Technol. 101 (September 2014) 121–132.
[24] I. Katsivalis, V. Signorini, F. Ohlsson, C. Langhammer, M. Minelli, L. Asp, Hydrogen permeability of thin-ply composites after mechanical loading, Compos. Appl. Sci. Manuf. 176 (2024) 107867.
[25] E. Szpoganicz, F. Hübner, U. Beier, M. Geistbeck, H. Ruckdäschel, Determination of tensile properties and damage onset of thin-ply CFRP laminates in cryogenic environments, in: Proceedings of the 21st European Conference on Composite Materials (ECCM21), Nantes, France, 2024 Jul.
[26] Y. Li, J. Meng, G. Niu, H. Yang, P. Wang, H. Lei, D. Fang, Cryogenic damage mechanisms of CFRP laminates based on in-situ X-ray computed tomography characterization, Compos. Sci. Technol. 247 (2024) 110413.
[27] K. Fujishiro, T. Ogasawara, K. Mizutani, H. Kumazawa, T. Aoki, Microscopic damage behavior in CFRP cross-ply laminates at cryogenic temperature, Compos. Sci. Technol. 256 (2024) 110774.
[28] P. Camanho, C. Dávila, S. Pinho, L. Iannucci, P. Robinson, Prediction of in situ strengths and matrix cracking in composites under transverse tension and in-plane shear, Compos. Appl. Sci. Manuf. 37 (2006) 165–176.
[29] G.J. Dvorak, N. Laws, Analysis of progressive matrix cracking in composite laminates II. First ply failure, J. Compos. Mater. 21 (4) (1987) 309–329.
[30] T.V. Parry, A.S. Wronski, The effect of hydrostatic pressure on transverse strength of glass and carbon fibre-epoxy composites, J. Mater. Sci. 25 (1990) 3162–3166.
[31] L.E. Asp, L.A. Berglund, R. Talreja, A criterion for crack initiation in glassy polymers subjected to a composite-like stress state, Compos. Sci. Technol. 56 (1996) 1291–1301.
[32] B. Fiedler, M. Hojo, S. Ochiai, K. Schulte, M. Ando, Failure behavior of an epoxy matrix under different kinds of static loading, Compos. Sci. Technol. 61 (2001) 1615–1624.
[33] L.E. Asp, L.A. Berglund, R. Talreja, Prediction of matrix-initiated transverse failure in polymer composites, Compos. Sci. Technol. 56 (1996) 1089–1097.
[34] S. García-Rodríguez, J. Costa, P. Maimí, V. Singery, I. Cózar, A. Quintanas-Corominas, A. Sasikumar, Experimental demonstration of the in-situ effect under transverse shear, Compos. Appl. Sci. Manuf. 138 (2020) 106047.
[35] T. Sebaey, J. Costa, P. Maimí, Y. Batista, N. Blanco, J. Mayugo, Measurement of the in situ transverse tensile strength of composite plies by means of the real time monitoring of microcracking, Compos. B Eng. 65 (2014) 40–46.
[36] A. Rafie, H. Madadi, A. Farrokhabadi, M. Herráez, In situ strength analysis of cross-ply composite laminates containing defects and interleaved woven layer using a computational micromechanics approach, Fatig. Fract. Eng. Mater. Struct. 44 (2021) 1225–1240.

[37] L. Canal, C. González, J. Segurado, J. Llorca, Intraply fracture of fiber-reinforced composites: microscopic mechanisms and modeling, Compos. Sci. Technol. 72 (2012) 1223–1232.
[38] M. Rodríguez, J. Molina-Aldareguía, C. González, J. Llorca, A methodology to measure the interface shear strength by means of the fiber push-in test, Compos. Sci. Technol. 72 (2012) 1924–1932.
[39] A. Pupurs, M.S. Loukil, E. Marklund, J. Varna, D. Mattsson, Transverse crack initiation in thin-ply laminates subjected to tensile loading at low and cryogenic temperatures, Mech. Compos. Mater. 59 (6) (2024) 849–860.
[40] I.G. García, V. Mantić, A. Blázquez, The effect of residual thermal stresses on transverse cracking in cross-ply laminates: an application of the coupled criterion of the finite fracture mechanics, Int. J. Fract. 211 (2018) 61–74.
[41] DIN 16459 – Determination of the Fiber Volume Content of fiber-reinforced Plastics by Thermogravimetric Analysis (TGA).
[42] ISO 6033 –Carbon Fibre Reinforced Plastics – Test Method – Determination of Interlaminar Fracture Toughness Energy – Mode I – G_{IC}.
[43] ISO 6034 –Carbon Fibre Reinforced Plastics – Test Method – Determination of Interlaminar Fracture Toughness Energy – Mode II – G_{IIC}.
[44] - ASTM D3039/D3039M-08 – Standard Test Method for Tensile Properties of Polymer Matrix Composite Materials.
[45] ASTM D3518/D3518M-18 – Standard Test Method for In-Plane Shear Response of Polymer Matrix Composite Materials by Tensile Test of a ±45° Laminate.
[46] Y. Chen, S. Wang, B. Liu, J. Zhang, Effects of geometrical and mechanical properties of fiber and matrix on composite fracture toughness, Compos. Struct. 122 (2015) 496–506.
[47] S. Oshima, A. Mamishin, M. Hojo, M. Nishikawa, N. Matsuda, M. Kanesaki, High-resolution in situ characterization of micromechanisms in CFRP laminates under mode II loading, Eng. Fract. Mech. 260 (2022) 108189.
[48] Y. Shindo, A. Inamoto, F. Narita, Characterization of mode I fatigue crack growth in GFRP woven laminates at low temperatures, Acta Mater. 53 (2005) 1389–1396.
[49] Y. Shindo, A. Inamoto, F. Narita, K. Horiguchi, Mode I fatigue delamination growth in GFRP woven laminates at low temperatures, Eng. Fract. Mech. 73 (2006) 2080–2090.
[50] Y. Shindo, T. Takeda, F. Narita, M. Miura, S. Watanabe, N. Koizumi, A. Idesaki, K. Okuno, Interlaminar shear properties of composite insulation systems for fusion magnets at cryogenic temperatures, Cryogenics 50 (2010) 36–42.
[51] I. Katsivalis, M. Persson, M. Johansen, F. Moreau, E. Kullgren, M. Norrby, D. Zenkert, S. Pimenta, L. Asp, Strength analysis and failure prediction of thin tow-based discontinuous composites, Compos. Sci. Technol. 245 (2024) 110342.